Acta Crystallographica Section D
Biological Crystallography
ISSN 0907-4449

Structural analysis of coniferyl alcohol 9-*O*-methyltransferase from *Linum nodiflorum* reveals a novel active-site environment

Stefan Wolters,[a] Manuel Neeb,[b] Anna Berim,[a] Johannes Schulze Wischeler,[b] Maike Petersen[a]* and Andreas Heine[b]*

[a]Institut für Pharmazeutische Biologie und Biotechnologie, Philipps-Universität Marburg, Deutschhausstrasse 17A, D-35037 Marburg, Germany, and [b]Institut für Pharmazeutische Chemie, Philipps-Universität Marburg, Marbacher Weg 6, D-35037 Marburg, Germany

Correspondence e-mail: petersen@staff.uni-marburg.de, heinea@mailer.uni-marburg.de

Received 21 November 2012
Accepted 28 January 2013

PDB References: coniferyl alcohol 9-*O*-methyltransferase, 4ems; complex with coniferyl alcohol, 4e70; complex with coniferyl alcohol 9-methyl ether and *S*-adenosyl-L-homocysteine, 4evi

Coniferyl alcohol 9-*O*-methyltransferase from *Linum nodiflorum* (Linaceae) catalyzes the unusual methylation of the side-chain hydroxyl group of coniferyl alcohol. The protein was heterologously expressed in *Escherichia coli* as a hexahistidine derivative and purified for crystallization. Diffracting crystals were obtained of the pure protein and of its selenomethionine derivative, as well as of complexes with coniferyl alcohol and with *S*-adenosyl-L-homocysteine together with coniferyl alcohol 9-*O*-methyl ether (PDB entries 4ems, 4e70 and 4evi, respectively). The X-ray structures show that the phenylpropanoid binding mode differs from other phenylpropanoid *O*-methyltransferases such as caffeic acid *O*-methyltransferase. Moreover, the active site lacks the usually conserved and catalytic histidine residue and thus implies a different reaction mode for methylation. Site-directed mutagenesis was carried out to identify critical amino acids. The binding order of coniferyl alcohol and *S*-adenosyl-L-methionine was investigated by isothermal titration calorimetry experiments.

1. Introduction

The methylation of secondary metabolites in plants is a very common reaction. Important roles of methylation reactions of secondary products in plants include, amongst many others, the production of volatile compounds to attract pollinators (Pichersky *et al.*, 2006) and the production of monolignols as building blocks for lignin and lignans (Neutelings, 2011). In recent years, studies of plant *S*-adenosyl-L-methionine (SAM) dependent small-molecule *O*-methyltransferases (SMOMTs) have been published with the aim of clarifying the amino acids required for catalytic activity and regioselectivity in the active site and to introduce a structure-based and mechanism-based classification system for a very divergent and large group of enzymes (Ferrer *et al.*, 2008; Lam *et al.*, 2007; Joshi & Chiang, 1998; Ibrahim *et al.*, 1998; Noel *et al.*, 2003). The most prominent common feature of the different SMOMTs is their utilization of SAM (Martin & McMillan, 2002; Roje, 2006). The sequence and structural motifs binding this substrate are highly conserved among many methyltransferases, although the substrates accepted for methylation and the methylation reaction mechanism itself can be very divergent. The SABATH family of methyltransferases is known to methylate the carboxyl and amino functions of phenylpropanoids (D'Auria *et al.*, 2003). Two additional classes of plant SMOMTs catalyze methylation reactions at phenolic hydroxyl functions of phenylpropanoids. The type I SMOMTs are enzymes with a molecular mass of ~40 kDa. They show a broad substrate acceptance and react independently of divalent cations. Examples are caffeic acid *O*-methyl-

transferases or isoflavone *O*-methyltransferases (Louie *et al.*, 2010; Zubieta *et al.*, 2001). In these SMOMTs the initial deprotonation of the substrate is carried out by a histidine side chain. In the case of caffeic acid *O*-methyltransferase the 3-*O* position is deprotonated to form a phenolate. Deprotonation is followed by nucleophilic attack of the phenylpropanoid at the activated methyl group of SAM, thus creating the methylated product. The type II SMOMTs usually have a lower molecular mass (~27–29 kDa) and are dependent on magnesium ions. They are predominantly known for the methylation of coenzyme A esters of the corresponding phenylpropanoids (Pakusch *et al.*, 1989). A member of this class is caffeoyl-CoA *O*-methyltransferase (CCoAOMT; Ferrer *et al.*, 2005), which methylates caffeoyl-CoA to produce feruloyl-CoA.

Modification of the lignin-polymer composition is a major focus for investigations of phenylpropanoid SMOMTs. By understanding the active-site configuration and discriminating function of some of the amino-acid side chains, substrate preferences can be modified or predicted using structural data (Gang *et al.*, 2002). By engineering SMOMT activities, lignin-polymer formation could be altered to obtain plants with better degradable lignin for animal feed or paper pulp production. Furthermore, the products of phenylpropanoid SMOMT reactions give rise to other secondary metabolites. One pathway, which can be found in the genus *Linum*, is the production of cytotoxic aryltetralin lignans (Kuhlmann *et al.*, 2002; Smollny *et al.*, 1998). In the course of our search for methyltransferases involved in lignan biosynthesis, we detected coniferyl alcohol 9-*O*-methyltransferase (Ca9OMT) in *L. nodiflorum* (Linaceae) and related *Linum* species (Berim *et al.*, 2007). The enzyme catalyzes the rather unusual methylation of the allylic side chain of a phenylpropanoid (Fig. 1). Novel methylation reactions could deliver new compounds that are of interest for pharmaceutical or nutritional use. The function of the product of the Ca9OMT reaction, coniferyl alcohol 9-*O*-methyl ether (C9M), in the plant is still the subject of ongoing research. Only a few reports of vicinal allylic methyl ethers in plants have been published to date. Coniferyl alcohol 9-*O*-methyl ether has been isolated from *Ligusticum wallichi* (synonym *L. chuangxiong*, Apiaceae; Naito *et al.*, 1992). The essential oil of *Agathosma ciliaris* (Rutaceae) contains the related compound *trans*-3,4-dimethoxycinnamyl alcohol methyl ether (Campbell & George, 1982). C9M can be found in plants and cell cultures of *L. nodiflorum* at amounts of up to 0.02% of the dry weight (Berim *et al.*, 2007). In this article, we report X-ray structures of Ca9OMT and present the structural characteristics of this side-chain-methylating enzyme. Since it is a novel reaction found in *L. nodiflorum* and other *Linum* species, the distinct structural modifications which were anticipated by sequence alignments of Ca9OMT with other SMOMTs are of interest. Despite the many conserved structural features found in Ca9OMT and other SMOMTs, certain differences such as the absence of the conserved catalytic histidine residue in the active site and the new phenylpropanoid-binding mode are observed and will be discussed here.

2. Materials and methods

2.1. Protein expression and purification

cDNA containing the full open reading frame of Ca9OMT from *L. nodiflorum* (EMBL accession No. DQ885221) was ligated into the *Nde*I and *Bam*HI restriction sites of the pET-15b expression vector (Novagen), which encodes a T7 promoter and adds an N-terminal hexahistidine tag to the protein, as described previously (Berim *et al.*, 2007). This plasmid was transferred into the expression host *Escherichia coli* BL21(DE3)pLysS for protein overproduction. The bacteria were grown at 310 K and 220 rev min^{-1} in 1 l LB medium containing 100 mg l^{-1} ampicillin as a selection marker to an optical density at 600 nm (OD_{600}) of 0.4. The overproduction of Ca9OMT was then induced by the addition of 1 m*M* isopropyl β-D-1-thiogalactopyranoside (IPTG) and the bacteria were cultivated for a further 5 h. The cells were harvested by centrifugation (3000*g*, 277 K) and frozen in liquid nitrogen. The cells were thawed on ice and resuspended in 6 ml lysis buffer (50 m*M* KH_2PO_4/K_2HPO_4 pH 8.0, 300 m*M* NaCl, 10 m*M* imidazole) followed by three rounds of sonication for 30 s. The homogenate was centrifuged for 30 min at 5000*g* and the clear supernatant was applied onto 0.5 ml Ni–NTA His-Bind resin (Novagen) in a disposable column and incubated for 1 h with slight shaking. After eight washing steps with 2 ml washing buffer 1 (50 m*M* KH_2PO_4/K_2HPO_4 pH 8.0, 300 m*M* NaCl, 20 m*M* imidazole) and two washing steps with 1 ml washing buffer 2 (50 m*M* KH_2PO_4/K_2HPO_4 pH 8.0, 300 m*M* NaCl, 50 m*M* imidazole), the protein was eluted with 3 × 1 ml elution buffer (50 m*M* KH_2PO_4/K_2HPO_4 pH 8.0, 300 m*M* NaCl, 250 m*M* imidazole). The combined final eluates were applied onto a PD10 desalting column (GE Healthcare) and the buffer was exchanged to 20 m*M* KH_2PO_4/K_2HPO_4 pH 7.0.

2.2. Concentration of protein preparations for crystallization

Protein concentrations were determined according to Bradford (1976). Washing and elution fractions were analyzed by SDS–PAGE essentially according to Laemmli (1970). The Ca9OMT elution fractions were pooled and concentrated to >10 mg ml^{-1} by ultrafiltration using Vivaspin 15 centrifugal concentrators (Sartorius Stedim Biotech) at 3000*g*.

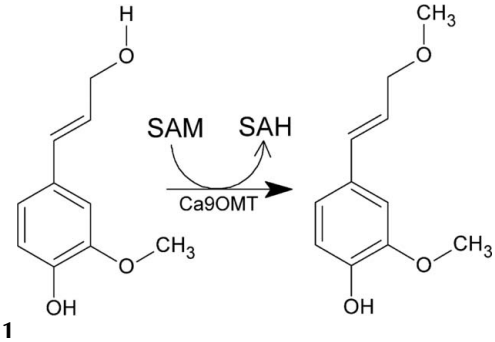

Figure 1
The reaction catalyzed by Ca9OMT. The activated methyl group of SAM is transferred to the allylic hydroxyl function of coniferyl alcohol to form the corresponding methyl ether.

2.3. Site-directed mutagenesis of Ca9OMT

Site-directed mutagenesis was carried out using the Agilent QuikChange II Site-Directed Mutagenesis Kit according to the manufacturer's instructions. Primers were designed using the online server software provided with the kit. The following mutations were generated using the pET-15b expression construct as template and corresponding mutagenesis primers: Y162F, C271H, C271S, C271A and D272N. The *E. coli* EZ (Qiagen) high-copy strain was transformed with the resulting PCR products, a plasmid preparation was carried out using a QIAprep MiniPrep Kit according to the manufacturer's instructions and the expression constructs were sequenced (Eurofins MWG Operon, Ebersberg, Germany) to check sequence integrity and the presence of the desired mutation. The mutated pET-15b expression vectors were subsequently transferred into *E. coli* BL21(DE3)pLysS and expression was carried out as described above.

2.4. Ca9OMT activity assay

The residual activities of the Ca9OMT mutants were checked using the established assay described previously by Berim *et al.* (2007). To detect small residual conversion rates, the incubation time was extended to 16 h. Representative chromatograms can be found as Supplementary Fig. S1[1].

2.5. Isothermal titration calorimetry

ITC experiments were performed using an ITC200 system (GE Healthcare, Northampton, Massachusetts, USA). ITC measurements were always performed using freshly prepared enzyme samples. The titration was carried out at 303 K and was started after a stable baseline had been achieved. The stirred sample cell initially contained the enzyme preparation (~100 µ*M*) and the syringe was loaded with a solution of the tested ligand (1 m*M*). For all solutions used in the ITC experiments the same batch of 20 m*M* KH_2PO_4/K_2HPO_4 pH 7.0 was used to minimize dilution peaks. The first injection of ligand solution was set to 0.3 µl and was not used in the integrated data analysis. Consecutive injections of 1.2–1.5 µl ligand solution were followed by 180–420 s intervals until saturation was observed. Four experimental setups were measured in triplicate.

(i) 98.06 µ*M* Ca9OMT in the stirred sample cell; addition of 1 m*M* coniferyl alcohol; Δt = 180 s; 1.2 µl per injection.

(ii) 80.54 µ*M* Ca9OMT and 180 µ*M* coniferyl alcohol in the stirred sample cell; addition of 1 m*M* SAM; Δt = 420 s; 1.2 µl per injection.

(iii) 98.06 µ*M* Ca9OMT in the stirred sample cell; addition of 2 m*M* SAM; Δt = 180 s; 1.2 µl per injection.

(iv) 81.55 µ*M* Ca9OMT and 340 µ*M* SAM in the stirred sample cell; addition of 1 m*M* coniferyl alcohol; Δt = 7 min; 1.2 µl per injection.

The resulting raw ITC data were integrated and analyzed using the *Origin* 7.0 software. A one-site binding model, as provided by the manufacturer, was used as a fitting model to determine the derived parameters. Representative curves from the four measurement setups can be found in Fig. 2.

2.6. Incorporation of selenomethionine into the Ca9OMT protein

A modified expression protocol (Doublié, 2007) was used to obtain a selenomethionine derivative of Ca9OMT. The expression vector (see above) was transferred into the methionine-auxotrophic *E. coli* D834 strain (Novagen). The growth medium was methionine-free supplemented M9 medium (Maniatis *et al.*, 1982) containing the following additives: $MgSO_4$ (2 m*M*), $CaCl_2{\cdot}2H_2O$ (2.5 m*M*), $FeSO_4$ (1 m*M*), all proteinogenic amino acids except for methionine at 40 mg l^{-1}, riboflavin, niacin amide, pyridoxine hydrochloride, thiamine (1 mg l^{-1} each), adenine, guanine, cytosine, thymine (1 mg l^{-1} each), glucose (4 g l^{-1}), ampicillin (100 mg l^{-1}) and selenomethionine (50 mg l^{-1}). Bacterial cultures for inoculation were grown in 10 ml LB medium (310 K, 220 rev min^{-1}, 16 h) and added to 1 l M9 growth medium. Cells were grown to an OD_{600} of 0.6 at 310 K and 220 rev min^{-1} followed by induction of protein overproduction by the addition of 1 m*M* IPTG and further cultivation at 310 K and 220 rev min^{-1} for 16 h. For purification, the same protocol was used as for the native protein. Because of the higher oxidation sensitivity of selenomethionine, all buffers were degassed by 30 min ultrasonication and 10 m*M* dithiothreitol was added to the washing and storage buffers.

2.7. Crystallization conditions for Ca9OMT

Initial crystallization assays were carried out using a Cartesian MicroSys SQ 4000 with standard crystallization screens. From several conditions with small crystals, two conditions could be reproduced: one condition was from the EasyXtal JCSG+ Screen from Qiagen (solution No. 49; 0.1 *M* sodium cacodylate pH 6.5, 1 *M* trisodium citrate) and the other was from the MBClass screen from Qiagen (solution No. 5; 1 *M* sodium/potassium phosphate pH 7.5, 0.7 *M* ammonium sulfate). Further crystallization experiments were carried out with the latter buffer system. Routinely, 1 µl buffer and 1 µl protein solution (~10 mg ml^{-1}) were mixed and incubated in a sitting-drop procedure with 500 µl reservoir volume in 24-well crystallization plates at 291 K. Without seeding, crystals suitable for X-ray diffraction experiments could be obtained in two to four weeks. On using streak-seeding, crystals grew in 2 d, when this was followed by macroseeding (Stura & Wilson, 1991; Bergfors, 2003) the time required to grow suitable crystals was significantly reduced. The crystals were flash-cooled in liquid nitrogen after a 1 min incubation in a 10 µl drop of cryoprotectant solution containing 25% glycerol in the crystallization buffer. Identical crystallization conditions were applied for the selenomethionyl protein and the complexes of Ca9OMT with substrates/products. To obtain complex crystals, stock solutions (1 mg ml^{-1}) of coniferyl alcohol, SAH or SAM were mixed and incubated at room temperature together with protein solution prior to the setup

[1] Supplementary material has been deposited in the IUCr electronic archive (Reference: MN5022). Services for accessing this material are described at the back of the journal.

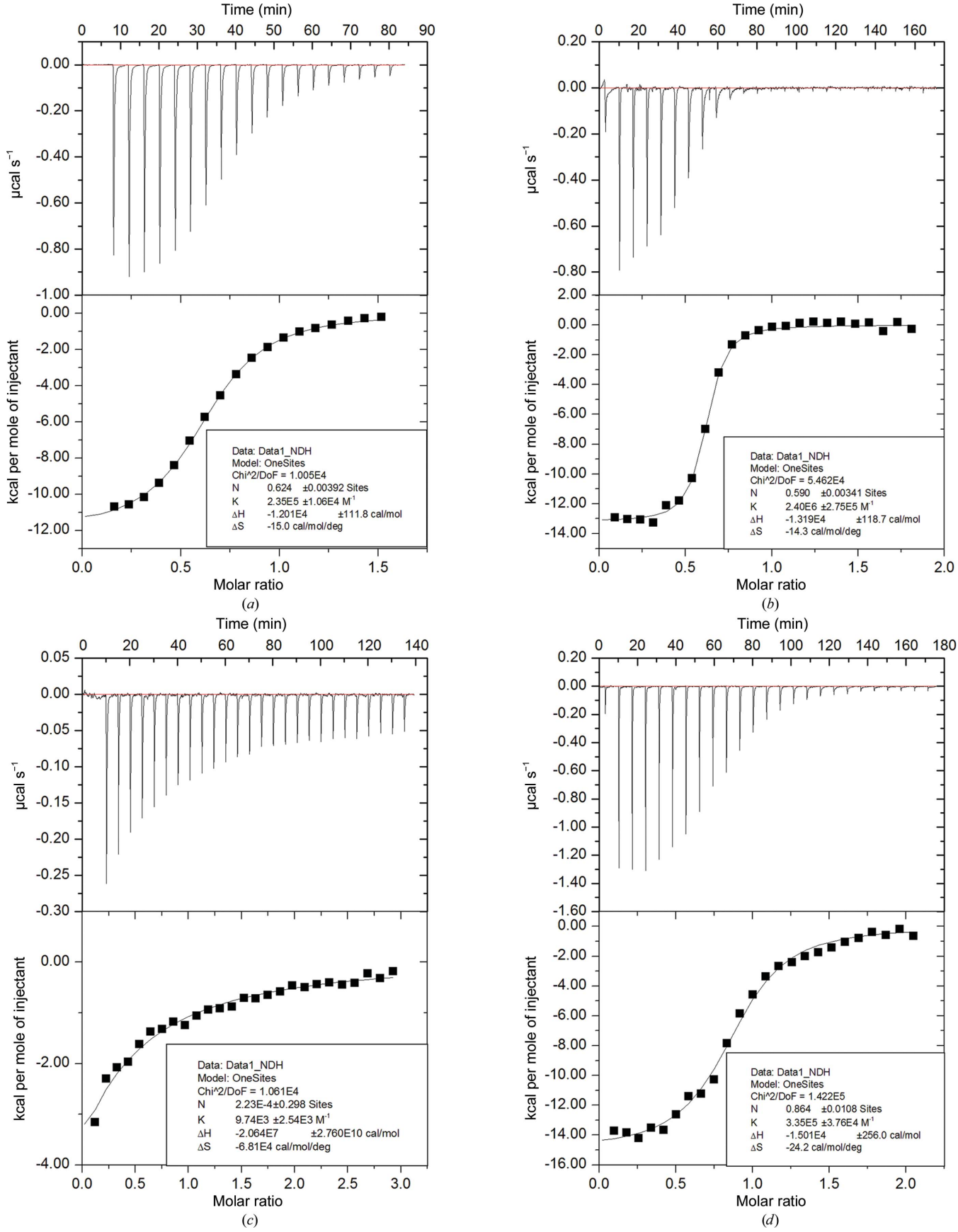

Figure 2
Representative ITC curves. Four measured experimental setups are compared: (*a*) setup (i), (*b*) setup (ii), (*c*) setup (iii), (*d*) setup (iv). See Supplementary Table S2 for details.

Table 1
Crystallographic data.

Values in parentheses are for the highest resolution shell.

	Native Ca9OMT (PDB entry 4ems)	Ternary complex (PDB entry 4evi)	Coniferyl alcohol complex (PDB entry 4e70)	Selenomethionine-derivative data set (for phasing)
Data collection				
Wavelength (Å)	0.91841	1.5418	0.91841	0.97971
Space group	$P2_12_12_1$	$P2_12_12_1$	$P2_12_12_1$	$P2_12_12_1$
Unit-cell parameters (Å)	a = 76.1, b = 104.6, c = 109.9	a = 75.9, b = 105.4, c = 109.0	a = 76.0, b = 104.5, c = 109.8	a = 76.4, b = 105.8, c = 110.0
Resolution range (Å)	30.00–1.75 (1.78–1.75)	10.00–2.02 (2.05–2.02)	30.00–1.61 (1.64–1.61)	50.00–2.30 (2.34–2.30)
Wilson B factor (Å^2)	18.3	23.4	19.6	25.2
No. of unique reflections	87649	57450	105779	39655
Multiplicity	4.4 (4.5)	5.2 (5.1)	5.2 (4.1)	4.9 (4.3)
$R_{\rm merge}$† (%)	6.1 (45.0)	9.1 (50.2)	4.0 (45.7)	10.9 (45.9)
Completeness (%)	98.9 (99.9)	99.8 (99.9)	98.1 (91.6)	98.9 (96.3)
$\langle I/\sigma(I)\rangle$	20.9 (3.0)	18.3 (3.3)	36.6 (2.8)	28.5 (3.9)
Refinement				
Resolution range	30.00–1.75	9.34–2.02	23.26–1.61	‡
No. of reflections used for refinement	83158	54343	100213	‡
$R_{\rm cryst}$§ (%)	16.4	17.6	17.0	‡
$R_{\rm free}$¶ (%)	19.0	20.3	19.1	‡
Refined residues	716	714	715	‡
Water molecules	629	449	666	‡
Ligand atoms	—	53	26	‡
R.m.s.d., angles (°)	1.11	1.09	1.13	‡
R.m.s.d., distances (Å)	0.007	0.006	0.007	‡
Ramachandran plot†† (%)				
Most favoured	94.5	93.9	93.9	‡
Additionally allowed	5.5	6.1	5.9	‡
Generously allowed	0	0	0.2	‡
Outliers	0	0	0	‡
Mean B (Å^2)				
All atoms	22.7	25.4	24.8	‡
Main chain	19.9	24.0	22.4	‡
Side chain	23.0	25.7	25.2	‡
Waters	33.2	31.5	33.5	‡
Ligands	—	23.1	24.9	‡

† $R_{\rm merge} = \sum_{hkl}\sum_i |I_i(hkl) - \langle I(hkl)\rangle|/\sum_{hkl}\sum_i I_i(hkl)$. ‡ The structure was only used for initial phasing and therefore was not further refined. § $R_{\rm cryst} = \sum_{hkl} ||F_{\rm obs}| - |F_{\rm calc}||/\sum_{hkl}|F_{\rm obs}|$. ¶ $R_{\rm free}$ was calculated as for $R_{\rm cryst}$ but using 5% of the data, which were excluded from refinement. †† Statistics from *PROCHECK* (Laskowski *et al.*, 1993).

of crystallization screens. The optimal ligand concentrations for crystallization were found to be 0.1–0.4 mg ml^{-1} (∼0.60–2.40 m*M*) for coniferyl alcohol and 0.1–0.2 mg ml^{-1} for SAH/SAM (∼0.25–0.50 m*M*) as final concentrations in the drop.

2.8. X-ray diffraction

Initial X-ray diffraction experiments were carried out using Cu $K\alpha$ radiation (1.54178 Å) from an Incoatec IμS microfocus sealed tube equipped with a MAR 345dtb image-plate detector. Higher resolution data sets were collected on the PSF beamline 14-2 at BESSY II (Berliner Elektronenspeicherring-Gesellschaft für Synchrotronstrahlung, Helmholtz-Zentrum für Energie, Berlin, Germany). Measurements were carried out at 100 K at a wavelength of 0.91841 Å. Data processing was carried out using *DENZO* and *SCALEPACK* as implemented in *HKL*-2000 (Otwinowski & Minor, 1997).

2.9. Experimental phasing by the SAD (single-wavelength anomalous dispersion) method

To obtain experimental phases by the SAD method, a data set was collected from a selenomethione-derivatized crystal at 0.97971 Å (peak) wavelength. Diffraction was recorded to 2.3 Å resolution with significant anomalous signal [d''/sig(d'') = 1.18–6.57] that allowed the determination of 24 out of 26 possible selenomethionine sites by *SHELXD* ($CC_{\rm max}$ = 52.0). SAD phasing was carried out using *SHELXE* (Sheldrick, 2008). An initial electron-density map could be calculated and a model (676 peptides, ten chains; longest chain 144 peptides; score 0.933) could be built *via ARP*/*wARP* (Langer *et al.*, 2008) as implemented in the *CCP*4 package (Winn *et al.*, 2011). For further model building the program *Coot* (Emsley *et al.*, 2010) was used in combination with the *PHENIX* package (Adams *et al.*, 2010) for refinement. Additional crystallographic details of data collection are included in Table 1.

2.10. Structure determination, model building and refinement

With the first macromolecular structure of Ca9OMT available, subsequent data sets were phased with the program *Phaser* (McCoy *et al.*, 2007) as implemented in the *CCP*4 suite in the automated molecular-replacement mode using an early model of Ca9OMT derived from the SAD structure as the template. Model building was carried out using the program *Coot* in combination with the *PHENIX* package as mentioned

above. Initial refinement steps were performed using rigid-body refinement and simulated-annealing routines with default parameters. Later stages included *xyz* refinement, TLS refinement, individual atomic displacement parameters (ADPs), occupancy refinement and the automatic addition of water molecules using default parameters. For fitting of amino-acid side chains and ligands, σ-weighted $2F_o - F_c$ and $F_o - F_c$ difference electron-density maps were used. A data fraction of 5% was used for R_{free} calculations. Model evaluation, representation and superposition was carried out using *PyMOL* (Schrödinger). Model validation was carried out using the programs *MolProbity* (Chen *et al.*, 2010) and *MOLEMAN* for *B*-value statistics (Kleywegt *et al.*, 2001). Hydrogen bonds and van der Waals contacts were assigned with the program *CONTACTSYM* (Sheriff *et al.*, 1987). The cutoff for hydrogen bonds and salt bridges was 3.4 Å and was up to 4.3 Å for van der Waals contacts, depending on the atom type and using standard van der Waals contacts. The solvent accessibility of individual residues was assessed using the program *MS* (Connolly, 1983) with a 1.4 Å radius for the solvent probe. Ramachandran plot statistics were produced with *PROCHECK* (Laskowski *et al.*, 1993). Additional crystallographic parameters are listed in Table 1.

3. Results

3.1. *De novo* structure determination of Ca9OMT

Ca9OMT was expressed in *E. coli* and protein carrying an N-terminal 6×His tag was purified by metal-chelate chromatography. Crystals were obtained in 0.5 *M* sodium/potassium phosphate pH 7.5 with 0.35 *M* ammonium sulfate using the sitting-drop method with 5 mg ml^{-1} purified protein and a reservoir volume of 500 µl at 291 K. Initial diffraction data were collected to 1.75 Å resolution for pure recombinant Ca9OMT protein with an N-terminal 6×His tag. The structure could not be determined by molecular-replacement methods using several different model structures and a variety of common molecular-replacement programs. Diffracting selenomethionine-containing crystals of Ca9OMT could be obtained as described by Doublié (2007). Single-wavelength anomalous dispersion (SAD) data delivered 24 out of 26 possible Se-atom sites. After subsequent phasing, these were used to calculate an initial electron-density map that enabled the building of an initial model of Ca9OMT (Fig. 3). At first sight, Ca9OMT shares many structural features with other plant SMOMTs described previously and annotated in the PDB (http://

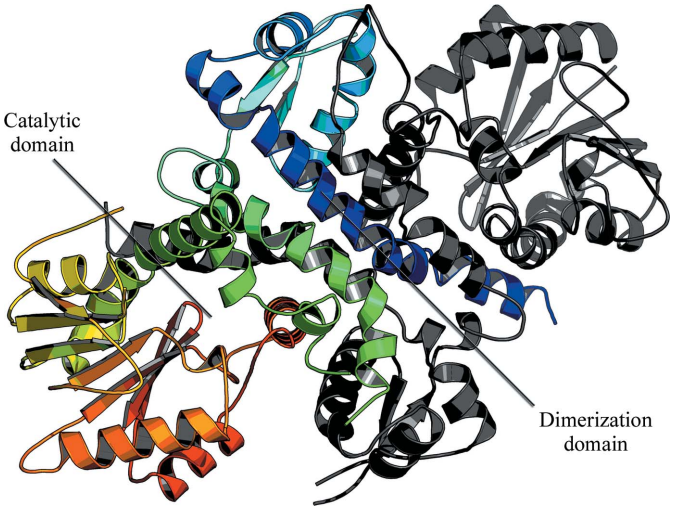

Figure 3
Structural overview of the homodimeric Ca9OMT. Monomer *A* is shown in rainbow colours from the N-terminus (blue) to the C-terminus (red); monomer *B* is depicted in grey.

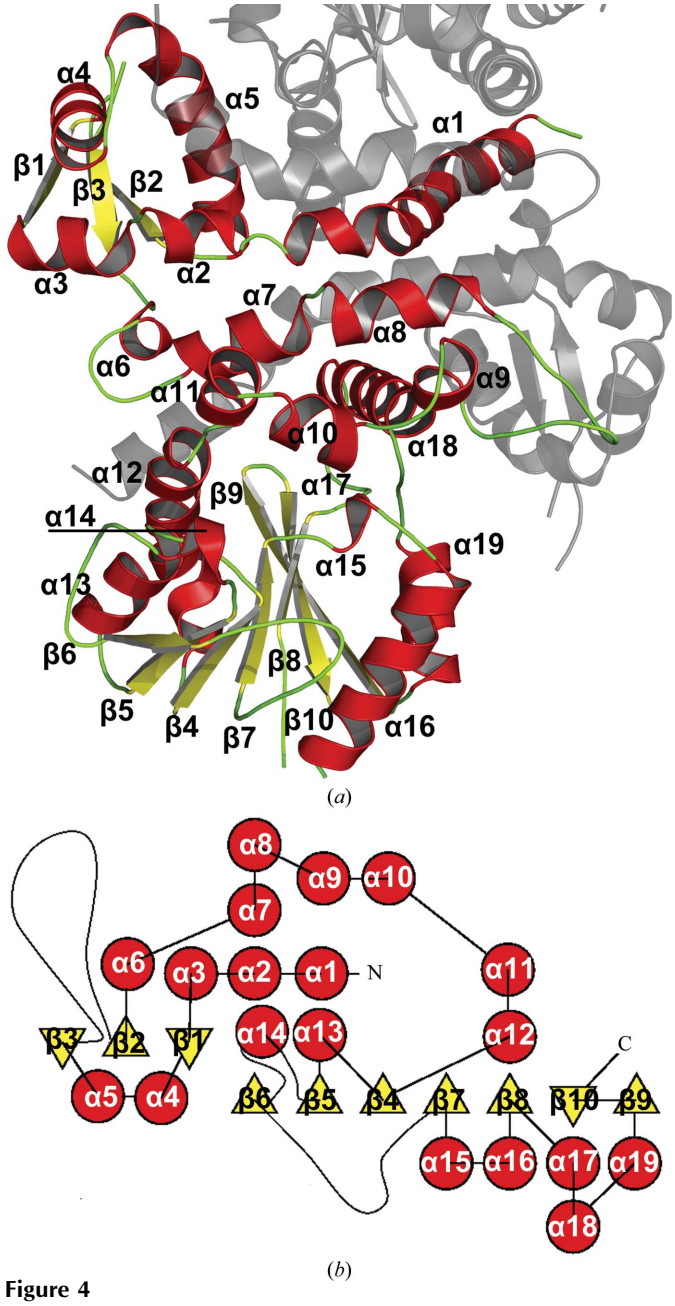

Figure 4
Schematic view of the secondary-structure elements in Ca9OMT. (*a*) Monomer coloured red for α-helices, yellow for β-strands and green for loops; the second monomer is shown in grey. (*b*) Corresponding topology diagram for the monomer: α-helices are shown as red circles and β-strands are shown as yellow triangles.

www.pdb.org), *e.g.* caffeic acid *O*-methyltransferase from *Lolium perenne* (PDB entry 3p9i; Louie *et al.*, 2010) and isoflavone *O*-methyltransferase from *Medicago sativa* (PDB entry 1fp2; Zubieta *et al.*, 2001). The enzyme is active as a homodimer. Each monomer consists of a large dimerization domain located at the N-terminus (residues 1–112) and a catalytic domain showing a Rossmann-fold-like architecture at the C-terminus (residues 113–368). Despite an amino-acid sequence similarity of only about 30–47%, the structure of Ca9OMT is highly similar to those of other plant SMOMTs, as shown by structural alignments (using the *DALI* server; Holm & Rosenström, 2010). The highest structural identities are observed for caffeic acid *O*-methyltransferase from *L. perenne* (PDB entry 3p9i; Louie *et al.*, 2010), isoflavone *O*-methyltransferase from *M. sativa* (PDB entry 1fp2; Zubieta *et al.*, 2001), caffeic acid/5-hydroxyferulic acid 3/5-*O*-methyltransferase from *M. sativa* (PDB entry 1kyz; Zubieta *et al.*, 2002) and isoflavone *O*-methyltransferase from *M. truncatula* (PDB entry 2qyo; C. Wang, X.-H. Yu & C.-J. Liu, unpublished work). *Z*-scores range from 33 to 37 and indicate very high structural similarity. Additionally, the structure of carminomycin 4-*O*-methyltransferase (DnrK) from *Streptomyces peucetius* (PDB entry 1tw3; Jansson *et al.*, 2004) will be discussed in comparison to Ca9OMT later.

The topology of Ca9OMT is shown in detail in Figs. 4(*a*) and 4(*b*). The topology diagram was calculated using the *TOPS* routine (Westhead *et al.*, 1999). The active site is formed by both monomers and thus dimerization is critical for activity, as described by Zubieta *et al.* (2001). The N-terminal helices α1, α2 and α3 (see Fig. 4*a*) are part of the rear wall of the active-site cavity in the second monomer. They also form a strong interface between the two monomers on the opposite side, with an approximate contact surface of 4800 Å^2 as calculated by *PISA* (Krissinel & Henrick, 2007). This large helical dimerization domain is followed by a small β-sheet (β1–β3) that is connected by two helices and a very long loop between residues 86 and 95. This loop cannot be modelled owing to high flexibility in the crystal. This is followed by seven helices (α6–α12) involved in interface formation between the monomers and formation of the binding pocket. The other side of the binding pocket together with the SAM-binding region is formed by a Rossmann-fold-like domain. This consists of seven β-strands (β4–β10) which are sandwiched between two helical layers (α11–α14 and α15–α18). Four residues of the uncleaved N-terminal His-tag linker are also visible in the crystal structure.

3.2. Ca9OMT complex structures

After structure determination of the native structure, crystals of complexes were obtained by cocrystallization in the presence of coniferyl alcohol and/or SAM. Very often crystals grew irregularly or as small two-dimensional plates. Successive seeding of small regular crystals (<100 µm in diameter) into fresh crystallization conditions led to large crystals (>200 µm in diameter). Crystals only grew at relatively low substrate concentrations (<3 m*M*), but the ligands were clearly defined in the electron density and the substrate-binding mode could be described.

Table 2
Coniferyl alcohol binding pocket.

The suffix B indicates an interaction with monomer *B*.

Residue	Interaction with coniferyl alcohol	Closest contact (Å)
Trp17B	Nonpolar cavity	4.7
Phe20B	Nonpolar cavity	3.3
Leu21B	Nonpolar cavity	3.9
Leu118	Nonpolar cavity	3.6
Cys121	Nonpolar cavity	3.6
Ser122	Hydrogen bond	2.7 and 2.9
Leu127	Nonpolar cavity	3.7
Phe175	Nonpolar cavity	3.9
Met179	π Interaction	3.8
Asp272	Hydrogen bond	2.5 and 3.1
Trp268	π Interaction	3.6
Cys271	Nonpolar cavity	4.0
Leu322	Nonpolar cavity	3.7
Leu325	Nonpolar cavity	3.6
Phe326	Nonpolar cavity	3.7
Phe329	Nonpolar cavity	3.8
Leu330	Nonpolar cavity	4.0

3.2.1. Phenylpropanoid binding mode. One data set at a resolution of 1.61 Å was obtained in which only coniferyl alcohol was bound in the active site (PDB entry 4e70). As presumed by early sequence alignments, the phenylpropanoid binding mode differs from those of other phenylpropanoid *O*-methyltransferases (Berim *et al.*, 2007). In contrast to the binding of substrate in caffeic acid *O*-methyltransferases (Zubieta *et al.*, 2002; Louie *et al.*, 2010), coniferyl alcohol binds in a 180° flip with the allylic hydroxyl function pointing towards the exit of the binding cavity. The 4-hydroxyl and 3-*O*-methyl functions of the phenylpropanoid are stabilized by Ser122 deep inside the binding pocket. The hydrophobic binding cavity is mostly formed by numerous nonpolar side chains (Table 2). Analysis by *MS* (Connolly, 1983) showed that

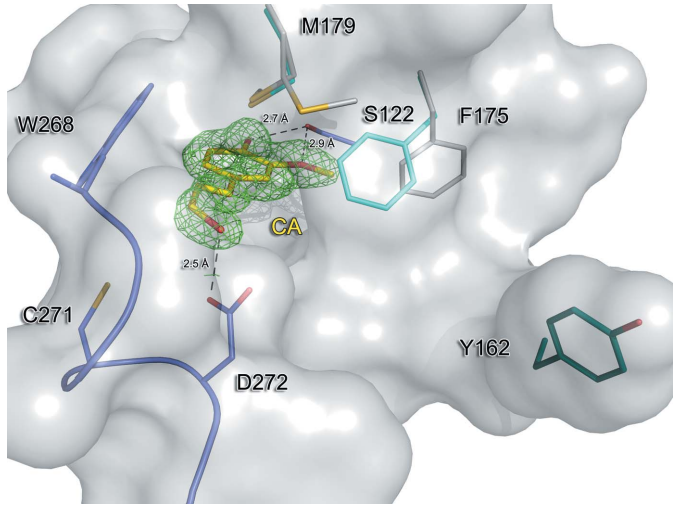

Figure 5
Binding of coniferyl alcohol (CA). CA is shown in yellow. The σ-weighted $F_o - F_c$ OMIT electron-density map is shown in green at the 3.0σ level (PDB entry 4e70).

the surface of coniferyl alcohol is almost completely buried in the binding pocket. The 9-hydroxyl function is coordinated by Asp272 (Fig. 5). In contrast to other SMOMTs, a catalytic histidine, which is normally responsible for deprotonation of the substrate, is not found in the vicinity of coniferyl alcohol. Instead, Cys271 is found at the position where the histidine is located in other SMOMTs, *e.g.* isoflavone *O*-methyltransferase from *M. sativa* (PDB entry 1fp2; Zubieta *et al.*, 2001). This implies a different reaction mechanism for Ca9OMT. There are also several changes in side-chain orientation on coniferyl alcohol binding compared with the native protein structure. Met179 is twisted inwards and stabilizes the allylic side chain and Phe175 also twists towards the substrate (an animated version of Fig. 5 has been deposited as Supplementary Material).

3.2.2. Ternary complex. A ternary-complex structure was obtained by cocrystallization of Ca9OMT with coniferyl alcohol and SAM (PDB entry 4evi). Data were collected to a resolution of 2.02 Å. The electron density for the substrates is well defined. The active site of monomer *A* is occupied by a product end state of the Ca9OMT reaction, while the active site of monomer *B* is only occupied by coniferyl alcohol. Considering the relatively low concentration of SAM compared with coniferyl alcohol in the final crystallization condition and the possibility of half-of-the-sites reactivity, this is not surprising (Levitzki & Koshland, 1976). The activated methyl group of SAM is not defined in the electron density. In contrast, there is a large difference electron density peak at oxygen 9 of coniferyl alcohol. This leads to the conclusion that the products C9M and *S*-adenosyl-L-homocysteine (SAH) are found in the structure. On binding of SAM, several conformational changes can be observed (Fig. 6). The C9M binding mode does not differ from the coniferyl alcohol binding mode. The highly conserved SAM-binding motifs are also found in Ca9OMT [*e.g.* the VDVGGG*X*G*X*T motif (residues 205–214) and the ADAVL*X*K motif (residues 261–267)]. Therefore, the SAM binding is almost identical to that previously described for SMOMTs (Zubieta *et al.*, 2002; Louie *et al.*, 2010). Some interactions are important for the observed conformational changes or methyl-group transfer and should be pointed out. The ribose ring is complexed by Asp231 and several polar interactions bridged by water molecules. As a consequence of these interactions, the regions around α15 and α10 are pulled ~3 Å towards the active site (indicated by the cyan arrows in Fig. 6). In consequence, Tyr162 is able to reach deep into the active site and to interact with Asp272 (Fig. 6). Tyr162 is also part of the nonpolar binding pocket that keeps the purine-ring system of SAH in place. Finally, the ring-bound O atom in the ribose moiety is coordinated by a bridged water interaction to Trp273 $N^{\varepsilon1}$ and Asp272 $O^{\delta2}$. Both substrates are coordinated to each other and the transferred methyl group at C9M can be found at a distance of 3.0 Å from the thioether function of SAM. A detailed figure (Supplementary Fig. S2) and an animation of the SAM binding mode can be found in the Supplementary Material. The SAM interactions are also listed in more detail in Supplementary Table S1.

3.3. Isothermal titration calorimetry (ITC) measurements

To investigate the substrate-binding order, ITC measurements were performed and the affinities of the substrates towards Ca9OMT were determined in four different experimental setups. ITC results are listed in Supplementary Table S2 and representative titration curves are shown in Fig. 2. The equilibrium dissociation constants (K_d) of the corresponding ligand–protein complexes were compared. The experiments showed that coniferyl alcohol binding is affected by SAM binding. The K_d is lowered by a factor of 1.8 compared with coniferyl alcohol binding in the absence of SAM (K_d of 5.26 *versus* 2.94 μM). Surprisingly, SAM binds very weakly without

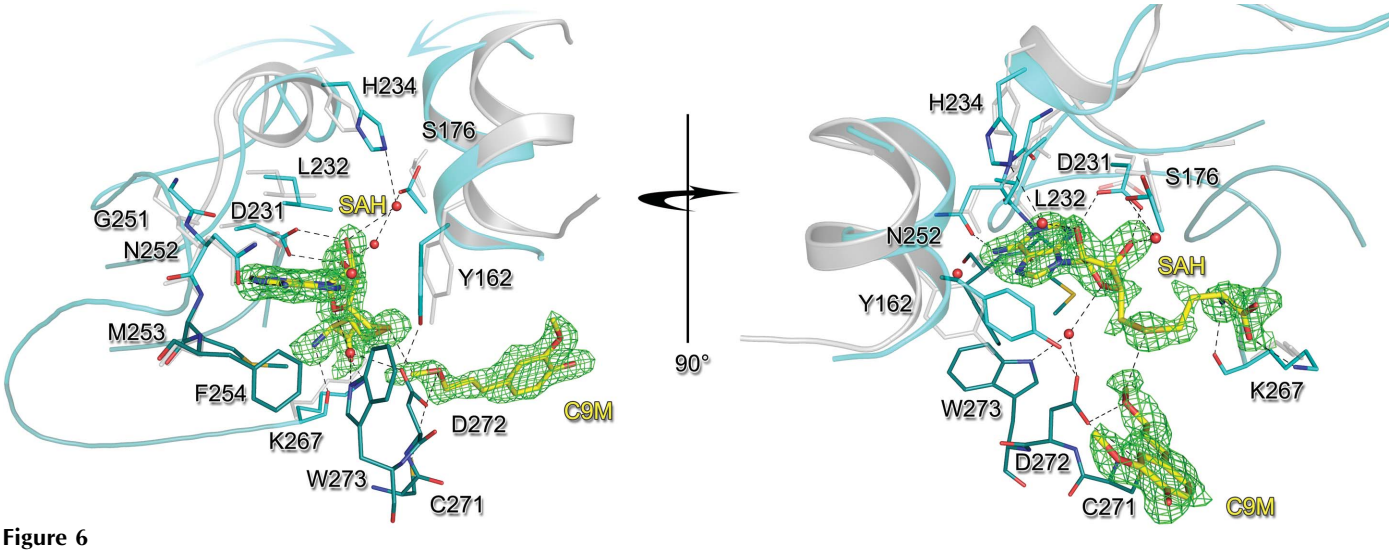

Figure 6
Ternary product complex with coniferyl alcohol 9-*O*-methyl ether (C9M) and SAH; there is a 90° clockwise rotation axis between the left and right illustrations. C9M and SAH are shown in yellow, the amino acids contributing to larger conformational changes are shown in light cyan, the native structure is shown in transparent light grey and the σ-weighted $F_o - F_c$ OMIT electron-density map is shown in green at the 3.0σ level. Conformational changes are indicated by cyan arrows.

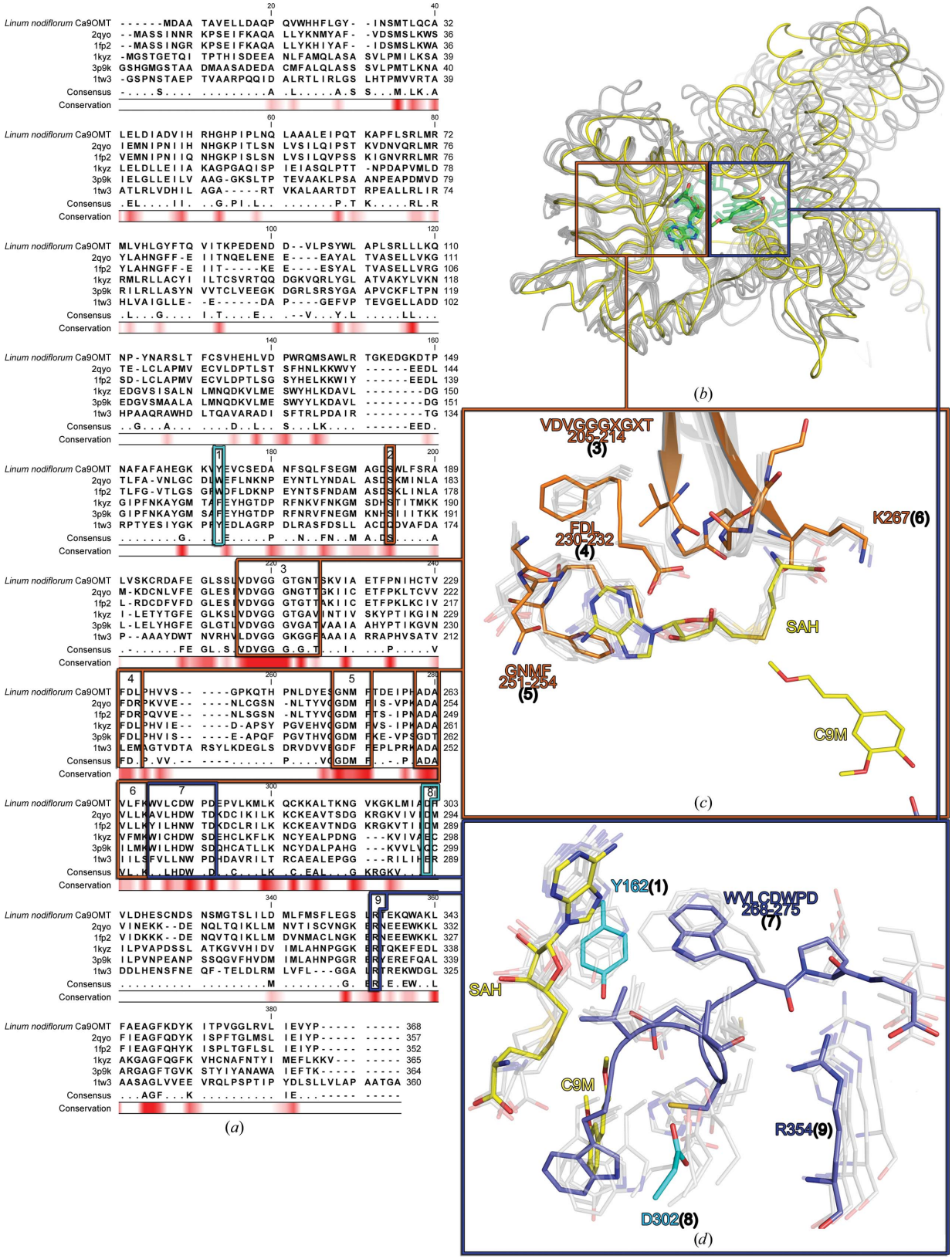

Figure 7
Sequence and structure alignment of several SMOMTs. (*a*) Sequence alignment of five SMOMTs (named by PDB code) with Ca9OMT. Important residues are marked by coloured boxes and are numbered (1) to (9); single conserved amino-acid side chains with possible important functions are shown in cyan, conserved SAM binding motifs are shown in orange and residues forming the catalytic centre are shown in blue. (*b*) Structural overlay of the SMOMTs shown in (*a*) as a C^{α} trace. Ca9OMT is shown in yellow, other structures are shown in grey and ligands are shown in green. (*c*, *d*) Structural alignment of SMOMT active sites in detail. C9M and SAH are shown in yellow; conserved sequence motifs are coloured and numbered corresponding to (*a*). Structurally conserved side chains and sequence motifs of other SMOMTs are shown as transparent overlays.

coniferyl alcohol bound first, as illustrated in Fig. 2(*c*). The high K_d value impaired its exact determination at the given SAM concentration of 1 m*M*. An exact value for K_d in experimental setup (iii) cannot be determined under the given conditions; however, a value in the range of 100 µ*M* or higher was estimated from our measurements. In contrast, SAM binding is enhanced by previously bound coniferyl alcohol by a factor of up to 222 (K_d of ∼100 µ*M* without coniferyl alcohol compared with a K_d of 0.45 µ*M* at saturating coniferyl alcohol concentrations).

3.4. Ca9OMT mutants

The Ca9OMT mutants C271A, C271S, C271H, D272N and Y162F were screened for residual catalytic activity. Only low methylation rates were observed for the C271S (46%), C271A (11%) and C271H (∼1%) mutants compared with wild-type Ca9OMT, whereas the D272N and Y162F mutants had no detectable activity; representative HPLC chromatograms are depicted in Supplementary Fig. S1.

4. Discussion

4.1. Sequence and structural alignment of Ca9OMT with other SMOMTs

The new phenylpropanoid binding mode and amino-acid sequence alignments implied distinct structural differences between Ca9OMT and other SMOMTs. The structure of Ca9OMT presented here shows strong structural parallels to other SMOMTs annotated in the PDB. Several structures are depicted as examples of a typical SMOMT and are compared with Ca9OMT by sequence and structural overlays (Figs. 7*a* and 7*b*). Initial amino-acid sequence alignments of Ca9OMT with other plant SMOMTs resulted in an identity ranging only between 29 and 47%. Despite this, the structural similarity among the SMOMTs is very high. The highly conserved and evolutionarily very old SAM-binding domain contributes strongly to this similarity. In Fig. 7(*a*) an amino-acid sequence alignment of structurally highly similar SMOMTs is shown in connection with a structural overlay. The overlay was achieved by superimposing the highly conserved SAM-binding domain (residues 205–214; VDVGGGTGNT) and SAM/SAH in each structure with that in Ca9OMT using *PyMOL* (Schrödinger; Fig. 7*b*). Obviously, the SAM-binding regions of the different structures are almost identical to each other. The catalytic amino acids and the residues complexing the substrate also correspond very well, even though only the SAM-binding domains were structurally aligned and the substrates differ considerably. However, the unique sequence deviations in Ca9OMT clearly show up in Fig. 7. The numbers (1) to (9) represent important structure/sequence features that can be found in Figs. 7(*a*), 7(*c*) and 7(*d*). The first difference from other plant SMOMT is Tyr162, where Ca9OMT shares an important structural feature with DnrK from *S. peucetius* (PDB entry 1tw3; Jansson *et al.*, 2004). As discussed later, Tyr162 (labelled 1 in Figs. 7*a* and 7*d*) must have at least a coordinating function in Ca9OMT and DnrK. In other plant SMOMTs aromatic amino acids are found here that stabilize the purine-ring system, but these do not interact with any residues involved in substrate/phenylpropanoid binding. Interestingly, they are located in almost the same orientation as Tyr162 in the structural overlay. The conserved Ser183 (labelled 2 in Fig. 7*a*; not shown in Fig. 7*c* for clarity) is involved in SAM coordination and complexes the carboxyl function of SAM. The VDVGGG*X*G*X*T motif (labelled 3 in Figs. 7*a* and 7*c*) is the most common motif in plant SMOMTs. Both the sequence and the structural overlay are highly conserved in this region. The bound SAM molecules are almost congruent in the structural overlay of six OMTs. In consequence, the residues responsible for strong SAM–protein interactions also only deviate minimally in positions such as, for example, Phe230, Asp231 and Leu232, while the sequence motif GNMF (251–254) undergoes a conformational change on SAM binding and is therefore quite flexible in the structural alignment (labelled 4 and 5 in Figs. 7*a* and 7*c*). Lys267 at the tip of β-strand 4 built by the ADAVL*X*K (261–267) motif also plays a major role in complexing the carboxyl function of SAM (labelled 6 in Figs. 7*a* and 7*c*). The structural overlay shows the preserved orientation of the sequence motif WVLCDWPD (labelled 7 in Figs. 7*a* and 7*d*). The residues found here surround the methylation site and contribute to both substrate and SAM binding. Furthermore, the most important catalytic residues in all SMOMTs are found in this region. In all shown SMOMT structural models except for Ca9OMT and DnrK the catalytic histidine is conserved in this position. Only Ca9OMT has Cys271 in the corresponding position. The clamping aspartate residues that usually interact with the missing histidine also superimpose in the overlay (Asp272 and Asp302; labelled 8 in Figs. 7*a* and 7*d*). The entire region is fixed in position by the highly conserved Arg335 (labelled 9 in Figs. 7*a* and 7*d*) which can be found in all aligned structures. An animated version of Fig. 7(*d*) has been deposited as Supplementary Material.

All of the motifs shown in Fig. 7 imply that SMOMTs can easily be identified by their conserved sequence motifs or by structural alignments. Superposition of all of the sequence motifs marked in Fig. 7(*a*) delivered r.m.s.d. values of between 0.6 and 0.8 Å. However, the identification or prediction of the substrate preferences of methyltransferases can be quite cumbersome because the size and shape of the active site is determined by several nonpolar amino-acid residues which determine substrate preference rather than certain polar interactions. It would be interesting to identify more methyltransferases that lack a catalytic histidine, especially in plants. The presented construction of the active-site environment may be crucial for certain substrates and/or different substrate-binding modes. Further studies will clarify the reaction mechanism by a combination of mutational and X-ray crystallographic studies.

4.2. ITC measurements

The obtained structural data showing the phenylpropanoid substrate deeply buried in the substrate-binding cavity implied

a different binding order of coniferyl alcohol and SAM compared with that of previously described SMOMTs (Huang *et al.*, 2004). The equilibrium complex dissociation constants determined by ITC show that SAM binds only weakly to the enzyme when the enzyme is not saturated with coniferyl alcohol. When coniferyl alcohol is already bound to Ca9OMT the affinity of the enzyme complex towards SAM is enhanced by a factor of up to 222. On the other hand, only a moderate improvement (a factor of 1.8) can be observed when the affinity of Ca9OMT towards coniferyl alcohol is compared between the enzyme–SAM complex and the enzyme alone. The gain in affinity towards coniferyl alcohol could also be explained by an apparent effect arising from substrate conversion. However, the large boost in substrate affinity towards SAM when coniferyl alcohol is bound first far exceeds the gain in substrate affinity in the opposite case. This strongly suggests a binding sequence in which the phenylpropanoid is bound first followed by SAM. In consequence, SAH should leave the active site first followed by the methylated product.

4.3. Substrate affinity and conformational changes

As already shown by ITC measurements coniferyl alcohol is expected to bind first, followed by SAM, which initiates several conformational changes and tightens the active-site cleft. The substrate-binding modes described above only deliver a snapshot of the reaction as it may occur in Ca9OMT. Conformational changes are critical for Ca9OMT to assure that the reaction can proceed. Met179, Phe175 and Tyr162 might play a key role in substrate preference and affinity towards educts and products of the methylation reaction. Without substrate, Met179 is flexible and is able to point towards the SAM-binding site exactly into the region of the activated methyl group of SAM, which might lead to a lower affinity towards SAM. This may be one of the reasons for the very low affinity towards SAM that was observed in the ITC measurements. Once coniferyl alcohol has bound Met179 flips inwards, forming a methionine–π interaction and opening space for SAM (Fig. 5). This probably leads to a higher affinity towards SAM, as also observed in ITC measurements. Tyr162 still seems to be very flexible under these conditions and is not capable of interacting with Asp272. Additionally, Phe175 flips towards the coniferyl alcohol. In the presence of SAM a tight conformation of Ca9OMT is induced (see Fig. 6). Tyr162 then points towards Asp272, closing the pocket around the adenosine ring, and the SAM-binding site adopts a conformation that keeps the adenosine ring tightly between the nonpolar side chains of Met253, Phe254 and Leu232. Both of the reactants are then in position for methyl transfer, in which Asp272 attracts the proton from coniferyl alcohol. The O atom of the allylic hydroxyl function attacks the positive charge of the activated methyl group, and an uncharged complex with lower affinity towards the coordinating amino-acid side chains is formed. On protonation of Asp272, the strong interaction with Tyr162 is weakened. Tyr162 is then again able to open towards the outer surface of the protein. Because of this, the adenosine ring is exposed to the surrounding solvent and SAH can leave the binding site. Once SAH has left the active site, C9M can be expelled from its cavity. The strong polar interactions at the tip of the phenylpropanoid side chain are now in the vicinity of the produced methyl ether, which has a much lower affinity towards Asp272. Furthermore, Met179 becomes flexible again because SAH has left the active site. Met179 flips outwards towards the empty SAM-binding site and the interaction between Met179 and the phenylpropanoid side chain is weakened. The conformation of Phe175 returns to the initial state and C9M can leave the active site and make room for a new molecule of coniferyl alcohol. A similar conformational change has also been observed in caffeic acid *O*-methyltransferase from *L. perenne* (PDB entry 3p9i; Louie *et al.*, 2010), where the authors state that the binding of SAM accommodated the binding pocket for the phenolic substrate, as described by Huang *et al.* (2004). In Ca9OMT, however, the substrate binding order is different, as implied by the structural data and ITC measurements: coniferyl alcohol must enter first into the binding pocket followed by SAM. The enzyme–coniferyl alcohol complex increases its affinity towards SAM tremendously and thus triggers the methylation reaction.

4.4. Proposed reaction mechanism and mutational studies of Ca9OMT

The composition of the active site depicted in the product state of Ca9OMT differs from those of other SMOMTs, *e.g.* caffeic acid *O*-methyltransferase from *L. perenne* (PDB entry 3p9i; Louie *et al.*, 2010), isoflavone *O*-methyltransferase from

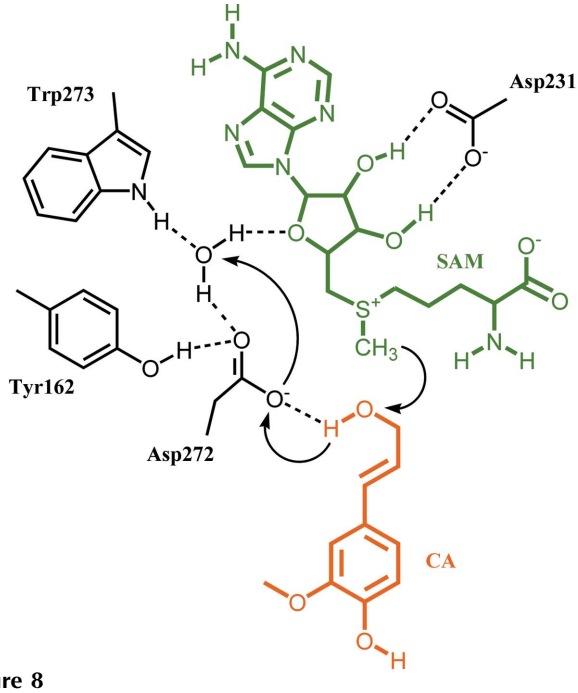

Figure 8
Schematic view of the active-site environment derived from the ternary-complex structure (PDB entry 4evi). SAH is shown in green, coniferyl alcohol is shown in orange and amino-acid side chains and a solvent water molecule are shown in black. Hydrogen-bond interactions are illustrated as black dashed lines. Possible group transfers are indicated by curved arrows.

M. sativa (PDB entry 1fp2; Zubieta *et al.*, 2001), isoflavone *O*-methyltransferase from *M. truncatula* (PDB entry 2qyo; C. Wang, X.-H. Yu & C.-J. Liu, unpublished work) and carminomycin 4-*O*-methyltransferase (DnrK) from *S. peucetius* (PDB entry 1tw3; Jansson *et al.*, 2004). Therefore, a different reaction mechanism is suggested for Ca9OMT deduced from the obtained data. The main differences are the lack of a histidine side chain in the vicinity of the methylation site of coniferyl alcohol, the switched orientation of the substrate, the different binding order and the substrate itself. In Ca9OMT not a phenolic but an allylic OH group needs to be deprotonated to enable methyl-group transfer. In other SMOMTs a phenolate ion is generated by deprotonation. A catalytic histidine clamped between two aspartate side chains is able to accept a proton from the phenylpropanoid substrate. The generated phenolate ion attacks the methyl group of SAM and generates the corresponding methyl ether and SAH (Zubieta *et al.*, 2001). In the initial state of this reaction the aspartate residues are deprotonated and are capable of stabilizing the protonated histidine. In the case of Ca9OMT there is no proton-accepting amino-acid side chain in the vicinity of the coniferyl alcohol hydroxyl function except for Asp272. Another potentially important residue is Tyr162, which is only able to interact with the catalytic amino acids after SAM binding. In the ternary-complex crystal structure (PDB entry 4evi) Tyr162 is well defined in the electron density compared with the other crystal structures (PDB entries 4e70 and 4ems), in which Tyr162 seems to be highly flexible, disordered and far away from the active site (Fig. 5). The hydroxyl function of Tyr162 keeps the aspartate side chain of Asp272 in place together with a highly complexed water molecule. The water molecule interacts with the ring-bound O atom of the ribose moiety of SAM and Trp273. Owing to these interactions the negatively charged carboxyl O atom of Asp272 is expected to point directly towards the allylic hydroxyl function of coniferyl alcohol and could attract its hydrogen (see Fig. 8 for an overview). As the reactive methyl group of SAM and the allylic hydroxyl function of coniferyl alcohol are brought into close vicinity, the O atom of the allylic hydroxyl function can attack the activated methyl group as a nucleophile. On deprotonation (mediated by Asp272) the methyl ether is generated and the proton is transferred to the solvent water. A similar composition of the active site has been described in carminomycin 4-*O*-methyltransferase from *S. peucetius* (PDB entry 1tw3), which also lacks a catalytic histidine in the active site (Jansson *et al.*, 2004). A leucine is found at the corresponding position instead of a histidine. Tyr142, which corresponds to Tyr162 in Ca9OMT, was also supposed to be active in catalysis. The mutation of Tyr142 to tryptophan resulted in a high residual catalytic activity (48%), suggesting only a coordinating function in this structure. For carminomycin 4-*O*-methyltransferase the explicit catalytic residues could not be determined and the authors concluded that DnrK is an entropic enzyme that utilizes proximity and orientation effects as major means of rate enhancement (Jansson *et al.*, 2004).

Based on the structural data, a catalytic role of Cys271 in Ca9OMT was anticipated. The clamping acidic aspartate residues (Asp272 and Asp302) are also present in Ca9OMT and Cys271 is located directly between these two side chains. However, initial mutational studies showed moderate residual activity when Cys271 was mutated to serine (C271S) or even to alanine (C271A). The conversion rates compared with wild-type Ca9OMT range from 46% for the C271S mutant down to 11% for the C271A mutant, indicating that Cys271 does not play an essential role in catalysis. Mutation of Cys271 to histidine (C271H) led to a very low residual activity, possibly owing to steric hindrance to coniferyl alcohol binding in the active-site cavity.

Mutation of Asp272 to asparagine (D272N) or of Tyr162 to phenylalanine (Y162F) resulted in a total loss of activity. This indicates a high relevance of these amino acids in the catalytic mechanism. In case of the D272N mutant the active site lacks a proton-acceptor function in the methyl-transfer region. Mutation of Tyr162 to phenylalanine hampers the interaction between Tyr162 and Asp272 and thus possibly prevents the enzyme from attaining the tight conformation of the active-site cleft. Thus, solvent water may not be sufficiently excluded from the active site, preventing activation of the coniferyl alcohol hydroxyl function. Additionally, the distance between the substrates could be significantly higher when the tight conformation is not achieved. Further investigation of the Ca9OMT mutants, including detailed kinetics and crystal structures, are still the subject of ongoing research.

We especially thank Professor Dr Gerhard Klebe (Institut für Pharmazeutische Chemie, Philipps-Universität Marburg) for providing the infrastructure and materials necessary for the X-ray crystallographic and ITC measurements as well as for fruitful discussions. We are grateful to the Helmholtz-Zentrum Berlin for the allocation of synchrotron-radiation beamtime and financial support and the beamline support staff for valuable assistance during data collection. We would also like to thank Professor Dr Klaus Reuter for initial support in the production of the selenomethionyl derivative.

References

Adams, P. D. *et al.* (2010). *Acta Cryst.* D**66**, 213–221.
Bergfors, T. (2003). *J. Struct. Biol.* **142**, 66–76.
Berim, A., Schneider, B. & Petersen, M. (2007). *Plant Mol. Biol.* **64**, 279–291.
Bradford, M. M. (1976). *Anal. Biochem.* **72**, 248–254.
Campbell, W. E. & George, P. (1982). *Phytochemistry*, **21**, 1455–1456.
Chen, V. B., Arendall, W. B., Headd, J. J., Keedy, D. A., Immormino, R. M., Kapral, G. J., Murray, L. W., Richardson, J. S. & Richardson, D. C. (2010). *Acta Cryst.* D**66**, 12–21.
Connolly, M. L. (1983). *Science*, **221**, 709–713.
D'Auria, J. C., Chen, F. & Pichersky, E. (2003). *Recent Adv. Phytochem.* **37**, 253–283.
Doublié, S. (2007). *Methods Mol. Biol.* **363**, 91–108.
Emsley, P., Lohkamp, B., Scott, W. G. & Cowtan, K. (2010). *Acta Cryst.* D**66**, 486–501.
Ferrer, J.-L., Austin, M. B., Stewart, C. & Noel, J. P. (2008). *Plant Physiol. Biochem.* **46**, 356–370.
Ferrer, J.-L., Zubieta, C., Dixon, R. A. & Noel, J. P. (2005). *Plant Physiol.* **137**, 1009–1017.
Gang, D. R., Lavid, N., Zubieta, C., Chen, F., Beuerle, T., Lewinsohn, E., Noel, J. P. & Pichersky, E. (2002). *Plant Cell*, **14**, 505–519.

Holm, L. & Rosenström, P. (2010). *Nucleic Acids Res.* **38**, W545–W549.
Huang, T.-S., Anzellotti, D., Dedaldechamp, F. & Ibrahim, R. K. (2004). *Plant Physiol.* **134**, 1366–1376.
Ibrahim, R. K., Bruneau, A. & Bantignies, B. (1998). *Plant Mol. Biol.* **36**, 1–10.
Jansson, A., Koskiniemi, H., Mäntsälä, P., Niemi, J. & Schneider, G. (2004). *J. Biol. Chem.* **279**, 41149–41156.
Joshi, C. P. & Chiang, V. L. (1998). *Plant Mol. Biol.* **37**, 663–674.
Kleywegt, G. J., Zou, J.-Y., Kjeldgaard, M. & Jones, T. A. (2001). *International Tables for Crystallography*, Vol. *F*, edited by M. G. Rossmann & E. Arnold, pp. 353–356. Dordrecht: Kluwer Academic Publishers.
Krissinel, E. & Henrick, K. (2007). *J. Mol. Biol.* **372**, 774–797.
Kuhlmann, S., Kranz, K., Lücking, B., Alfermann, A. & Petersen, M. (2002). *Phytochem. Rev.* **1**, 37–43.
Laemmli, U. K. (1970). *Nature (London)*, **227**, 680–685.
Lam, K. C., Ibrahim, R. K., Behdad, B. & Dayanandan, S. (2007). *Genome*, **50**, 1001–1013.
Langer, G., Cohen, S. X., Lamzin, V. S. & Perrakis, A. (2008). *Nature Protoc.* **3**, 1171–1179.
Laskowski, R. A., MacArthur, M. W., Moss, D. S. & Thornton, J. M. (1993). *J. Appl. Cryst.* **26**, 283–291.
Levitzki, A. & Koshland, D. E. (1976). *Curr. Top. Cell. Regul.* **10**, 1–40.
Louie, G. V., Bowman, M. E., Tu, Y., Mouradov, A., Spangenberg, G. & Noel, J. P. (2010). *Plant Cell*, **22**, 4114–4127.
Maniatis, T., Fritsch, E. F. & Sambrook, J. (1982). *Molecular Cloning: A Laboratory Manual.* New York: Cold Spring Harbor Laboratory Press.
Martin, J. L. & McMillan, F. M. (2002). *Curr. Opin. Struct. Biol.* **12**, 783–793.
McCoy, A. J., Grosse-Kunstleve, R. W., Adams, P. D., Winn, M. D., Storoni, L. C. & Read, R. J. (2007). *J. Appl. Cryst.* **40**, 658–674.
Naito, T., Niitsu, K., Ikeya, Y., Okada, M. & Mitsuhashi, H. (1992). *Phytochemistry*, **31**, 1787–1789.
Neutelings, G. (2011). *Plant Sci.* **181**, 379–386.
Noel, J. P., Dixon, R. A., Pichersky, E., Zubieta, C. & Ferrer, J.-L. (2003). *Recent Adv. Phytochem.* **37**, 37–58.
Otwinowski, Z. & Minor, W. (1997). *Methods Enzymol.* **276**, 307–326.
Pakusch, A. E., Kneusel, R. E. & Matern, U. (1989). *Arch. Biochem. Biophys.* **271**, 488–494.
Pichersky, E., Noel, J. P. & Dudareva, N. (2006). *Science*, **311**, 808–811.
Roje, S. (2006). *Phytochemistry*, **67**, 1686–1698.
Sheldrick, G. M. (2008). *Acta Cryst.* A**64**, 112–122.
Sheriff, S., Hendrickson, W. A. & Smith, J. L. (1987). *J. Mol. Biol.* **197**, 273–296.
Smollny, T., Wichers, H., Kalenberg, S., Shahsavari, A., Petersen, M. & Alfermann, A. W. (1998). *Phytochemistry*, **48**, 975–979.
Stura, E. A. & Wilson, I. A. (1991). *J. Cryst. Growth*, **110**, 270–282.
Westhead, D. R., Slidel, T. W. F., Flores, T. P. J. & Thornton, J. M. (1999). *Protein Sci.* **8**, 897–904.
Winn, M. D. *et al.* (2011). *Acta Cryst.* D**67**, 235–242.
Zubieta, C., He, X., Dixon, R. A. & Noel, J. P. (2001). *Nature Struct. Mol. Biol.* **8**, 271–279.
Zubieta, C., Kota, P., Ferrer, J.-L., Dixon, R. A. & Noel, J. P. (2002). *Plant Cell*, **14**, 1265–1277.